



Soft Matter

Time-dependent Shear Rate Inhomogeneities and Shear Bands in a Thixotropic Yield-Stress Fluid under Transient Shear

Journal:	<i>Soft Matter</i>
Manuscript ID	SM-ART-05-2019-000902.R2
Article Type:	Paper
Date Submitted by the Author:	01-Sep-2019
Complete List of Authors:	Wei, Yufei; University of Michigan, Chemical Engineering Solomon, Michael; University of Michigan, Chemical Engineering Larson, Ronald; University of Michigan, Chemical Engineering

SCHOLARONE™
Manuscripts

ARTICLE

Time-dependent Shear Rate Inhomogeneities and Shear Bands in a Thixotropic Yield-Stress Fluid under Transient Shear

Yufei Wei,^a Michael J. Solomon^a and Ronald G. Larson^{a*}

Received 00th January 20xx,
Accepted 00th January 20xx

DOI: 10.1039/x0xx00000x

We study the rheological responses and shear-rate inhomogeneities and shear banding behaviors of a thixotropic fumed silica suspension in shear startup tests and flow reversal tests. We find that this suspension under transient shear exhibits not only viscoelasticity, yielding, kinematic hardening, and thixotropy, but also time-dependent shear inhomogeneities including bands when the apparent shear rate is below a critical value between 0.1 and 0.25 s⁻¹. Through multiple shear startup tests and flow reversal tests, we find that thixotropy promotes flow heterogeneity while kinematic hardening suppresses it. We propose a simple thixo-plastic constitutive equation that can qualitatively predict the important features of the rheological response and banding dynamics in shear startup tests and flow reversal tests.

Introduction

Thixotropic yield-stress fluids (TYSFs) are very common and include attractive emulsions¹, pastes², microgels³, and colloidal suspensions⁴⁻⁶. Flow can induce slow structural changes in TYSFs – structure breakup and growth, also referred to as shear rejuvenation and aging – the latter driven by Brownian motion or interactions that induce relative motion of particles⁷. TYSFs, therefore, often show slow time-dependent and reversible rheological behavior, such as a gradual decrease in the apparent viscosity after flow starts or increases in rate, and an increase in viscosity after flow stops or decreases.

The strong couplings between internal structures and flow in TYSFs often lead to inhomogeneous velocity gradients, in which a macroscopically homogeneously sheared fluid develops variations in the shear rate across the sample. In the extreme case, the flow field separates into layers or “bands,” each of distinctly different shear rate. In other cases, the variations in shear rate are less dramatic, although sometimes developing over time into distinct bands, each with a well-defined shear rate.⁸⁻¹³ Shear banding and other shear rate inhomogeneities occur in various flow regimes and can greatly alter the measured rheology.⁸⁻¹³ Understanding the occurrence and evolution of shear rate inhomogeneities is crucial to interpreting bulk rheological data and in the design of processing flows that enhance or mitigate these effects as needed. The interplay between time scales of rheology and shear rate inhomogeneities in TYSFs is drawing growing attention but remains far from being adequately understood. We note that “shear banding” and “shear rate inhomogeneity” are often not clearly differentiated in the literature. Here, while

not defining precisely what degree of uniformity in shear rate is required within a single region to justify calling it a “band” rather than a “shear rate inhomogeneity,” we will refer to gradual changes in shear rate across the sample as “inhomogeneities,” while reserving the term “shear band” for a defined region with a nearly uniform shear rate. The simplest “shear banding” occurs when a part of the domain is solid-like with zero shear rate and the other part is flowing with a nearly uniform shear rate. This corresponds to a sample that is yielded in one region, and the remainder unyielded, which can occur in even the simplest thixotropic yield-stress fluids.

Most studies of TYSFs focus on *steady-state* shear bands and inhomogeneities. The few works reporting time-dependent shear bands and inhomogeneities show that different TYSFs exhibit very different behaviors. Martin and Hu,¹⁴ for example, reported that aged Laponite suspensions form transient shear rate inhomogeneities after shear startup, that in some cases evolve into two distinct bands, one with a nearly uniform shear rate, and the other essentially a stationary plug; i.e., yielded and unyielded domains, as discussed above. Dimitriou and McKinley¹⁵ reported more complex shear rate inhomogeneities in a thixotropic waxy crude oil where velocity profiles fluctuate irregularly at a constant macroscopic apparent shear rate. The authors observed a critical shear rate above which the flow always remains uniform. Divoux et al.¹² studied shear inhomogeneities and banding in several TYSFs in shear-rate-ramp experiments. They found that both the hysteresis area in the flow curves (A_σ) and the degree of inhomogeneity in the shear rate (A_v) depend strongly on the sweep rate of the shear rate, $(\delta t)^{-1}$. A_σ and A_v exhibit a maximum at a critical value of δt . This phenomenon is seen in several TYSFs including mayonnaise, carbon black suspensions, and Carbopol gels. This robust maximum indicates that both the bulk rheology and the “banding” dynamics depend strongly on an intrinsic material restructuring time. Kurokawa et al.¹⁶ studied the behavior of relatively distinct banding with one of the two bands typically

^a Department of Chemical Engineering, University of Michigan,

^b Ann Arbor, MI, USA. E-mail: rlarson@umich.edu

Electronic Supplementary Information (ESI) available: [details of any supplementary information available should be included here]. See DOI: 10.1039/x0xx00000x

immobile or unyielded, in an attractive gel composed of non-Brownian fumed silica colloids. Their flow procedure consisted of a preshear, a rest period of a duration t_w , and a shear startup at a shear rate $\dot{\gamma}$. They observed steady shear banding when $\dot{\gamma}$ is smaller than a critical value $\dot{\gamma}^*$ and transient shear banding when $\dot{\gamma} > \dot{\gamma}^*$. Moreover, $\dot{\gamma}^*$ depend on t_w as well as the geometry of the flow cell. During transient banding processes, the stress response exhibits a multiple-step relaxation pattern with successive peaks. The authors found that this phenomenon is caused by the occurrence of avalanche-like fluidization events that are distributed heterogeneously along the vorticity direction. The local avalanche-like fluidization also leads to large peaks in the slip velocity.

While TYSF suspensions often show profoundly complex time-dependent phenomena, as discussed above, some polymeric and surfactant solutions show shear inhomogeneities and banding that are simpler and more easily explained. An interesting example is a study by Hu and Lips¹⁷ who showed the gradual development of two distinct bands, both with non-zero shear rate, from an initial uniform shear rate in a solution of worm-like micelles. The development of the bands occurs through a gradual time-dependent increase in shear rate at one wall and decrease at the other, a process they call “shear tilting.” Only as this tilting comes to a conclusion do two distinct bands, each with nearly uniform shear rate, finally appear. This evolution was traced to micelle entanglement/disentanglement dynamics.

Another interesting study of gradual band formation has been observed by Rogers et al.¹⁸ in a suspension of “soft, glassy particles” consisting of many-arm star polymers. In this case, a smooth velocity profile in a circular Couette geometry gradually evolves into a non-flowing “band” at the outer cylinder and a flowing one at the inner cylinder, which they explained by a simple time-dependent fluidity model.

Recent years have also seen remarkable progress in theoretical studies on shear banding in TYSFs. Fielding and coworkers^{9-11, 19} have carried out extensive theoretical studies of the criteria and dynamics of shear bands in time-dependent flows including shear startup, step stress, rapid strain ramp, and large amplitude oscillatory shear using simple model constitutive equations. The recent work of Radhakrishnan et al.²⁰ showed that the findings of Divoux et al.¹² as discussed earlier can be qualitatively predicted by a fluidity model and a soft glassy rheology model.²¹ Although most theoretical work to date has been based on phenomenological constitutive models, Martens et al.²² have recently made some initial steps towards developing a mesoscopic model based on local plastic events, which produce long-range stress re-distribution, and steady-state shear bands.

Despite the rapid progress as reviewed above, large gaps in the understanding of shear banding in TYSFs remain. TYSFs include enormously many materials, and their practical flow involves a wide range of regimes. The few works discussed above show that the rheological responses and banding behaviors of TYSFs strongly depend on factors such as material composition, preparation procedures, and flow regimes.

Additional studies on this topic are critically needed to better understand TYSFs. Another limitation of current studies is the shortage of constitutive models that can predict both rheological responses and banding or inhomogeneous shear behaviors. Thus, despite recent progress^{4, 15, 23-25}, it remains unknown whether, or how well, those constitutive models can predict the banding dynamics of TYSFs.

In the present work, we study the evolution of shear inhomogeneities and bands in a thixotropic fumed silica suspension under transient shear. This type of suspension was originally developed by Dullaert and Mewis²⁶ as a model thixotropic fluid. It is made by dispersing a hydrophobic fumed silica (radius of primary particle, 16 nm) in a non-volatile medium composed of a high boiling paraffin oil and low-molecular-weight polymer. The polymer is added to viscosify the solvent. Aggregation of fumed silica particles gives rise to rich rheological behaviors including thixotropy, viscoelasticity, kinematic hardening, and yielding. Dullaert and Mewis focused on thixotropy and studied the rheological response of this material in shear-rate-jump experiments.²⁶⁻²⁸ They proposed a structural kinetics model that can quantitatively predict those rheological responses.²⁹ Armstrong et al.²³ studied a very similar suspension with an emphasis on more complex shear histories such as shear reversal, oscillatory shear, and unidirectional shear ramp. Two constitutive models have been proposed based on this dataset – a structural kinetics model by Armstrong et al.²³ and a coarse-grained population balance model by Mwasame et al.²⁴ Our recent works^{4, 25} show that fumed silica suspensions show thixotropic relaxation with multiple timescales and kinematic hardening under flow histories involving changes of shearing direction. We proposed a constitutive model with the two features and showed that this model gives quantitative predictions over a wide range of shear histories²⁵.

Despite extensive rheological study of fumed silica suspensions such as these, no study has been made of their velocity profiles under shear. To correctly interpret the rheological data, it is critical to know whether this material forms bands or inhomogeneities in shear, and if it does, how the velocity profile evolves under different shear histories. In this work, we for the first time study the time-dependent velocity profile in this fluid through time-resolved particle image velocimetry (PIV). We use a novel PIV method designed specifically for one-dimensional (1D) shear flows that provides high spatial resolution and allows the examination of the velocity profile in fine detail. With this new PIV method, we study quantitatively how flow inhomogeneities evolve with time in shear startup experiments and shear reversal experiments. The combination of shear startup and flow reversal provides interesting insights into the dynamics of flow inhomogeneities under transient shear. In addition to the experimental study, we propose a minimal model to predict qualitatively the banding dynamics.

The remainder of this paper is organized as follows. First, we introduce the materials and methods. Then, we discuss the experimental results. Next, we present a constitutive model and

solve it for 1D shear flow with similar shear histories as used in rheological measurements. We compare the numerical simulations with experimental results. We then summarize the results and discussion.

Materials and methods

Materials and instruments

The material we study is based on a model thixotropic system developed by Dullaert and Mewis²⁶. It has three components – a hydrophobic fumed silica (2.9 vol%, R972, Evonik Industries), a low-molecular-weight poly(isobutylene) (27.0 wt%, calculated on total sample mass, Oppanol-B3, BASF), and a high boiling paraffin oil (65.9 wt% 18512 Sigma-Aldrich). The fumed silica particles have a primary radius of 16 nm and are aggregated into micron-sized agglomerates²³. When dispersed in paraffin oil, the agglomerates further aggregate and form weak internal structures, which gives rise to rich rheological behaviors including thixotropy, viscoelasticity, and yielding. The polymer can reduce the interparticle attraction due to polymer adsorption on the silica surface. By adjusting the percentage of the polymer, one can manipulate the thixotropic recovery time scales. The polymer also increases the viscosity of the medium fluid. Due to the low molecular weight, the depletion effect is insignificant. The paraffin oil provides a non-volatile Newtonian medium. The readers may refer to the work of Dullaert and Mewis²⁶ for a further discussion on how to tune the rheological properties of this suspension by adjusting the percentages of the components.

We use a slightly different formula of the suspension – fumed silica (7.1 wt%, corresponding to 2.9 vol%, R972, Evonik Industries), polybutene oligomer (28.8 wt%, Indopol H-25, Mn = 635, INEOS), and paraffin oil (64.1 wt%, 18512 Sigma-Aldrich). Note that the polymer differs from that used by Dullaert and Mewis due to its availability. Our recent works^{4, 25} show that the rheological behaviors of this suspension are qualitatively similar to those of the original suspension developed by Dullaert and Mewis. The rheological data of the linear viscoelastic behaviors of the suspension can be found in the supplementary materials (Figs. S15-S17). More details regarding the preparation procedure of this suspension can be found in our recent work⁴.

To measure local velocity profiles, we seed fluorescent particles (0.1 vol%, radius = 1.5 μm , Fluoresbrite-YG, Polysciences) into this suspension. The fluid is homogenized using a Cole-Palmer ultrasonic processor (5 min, 500W, 20 kHz) and then put on a bottle roller (9 rpm, Thermo Scientific) for ten days. Before measurement, the suspension is homogenized again through the Cole-Palmer ultrasonic processor (1 min, 500W, 20 kHz) and then is centrifuged at 500 g for 10 seconds to remove air bubbles. The second homogenization prior to rheological tests is important and skipping this step leads to noticeable differences in the rheological response of this suspension, as shown in the supplementary materials (Fig. S7).

A control fluid was made to test the PIV setup. This fluid is made by seeding tracer particles into the suspending medium (31 wt% polybutene oligomer, 69 wt% paraffin oil) of the fumed

silica suspension. This control fluid is a Newtonian fluid with a viscosity of 0.24 Pa·s at 25 °C.

We use the MCR 702 rheometer (Anton Paar) with cone and plate geometry (cone angle 2°, diameter 50 mm, truncation gap 210 μm) to measure the rheology. The geometry is made of stainless steel and has smooth surfaces. A fluorescence microscope (Module 1, band pass 450–490 nm, provided by Anton Paar) that views the sample through its edge meniscus is used to record movements of tracer particles in the velocity – velocity gradient plane. The microscope is mounted on a stage that can be moved horizontally and vertically by two micrometer drives. The focal plane of the objective lens lies 0.1 mm inside the sample-air interface. Fig. 1(a) shows a brief schematic diagram of the instruments. A more detailed one is provided in the supplementary materials (Fig. S1). During rheological measurement, a CCD camera (Lm165C; resolution, 1392 x 1040 pixels; made by Lumenera) connected to the fluorescent microscope records at a frame rate of 15 frames per second (or higher rates at lower resolutions). All rheo-PIV experiments were performed at room temperature that fluctuates between 22 and 23°C.

PIV algorithm

This section provides details of our algorithm for the time-resolved PIV. The 1D velocity profile at any time t , $v_x(y,t)$, is calculated based on a pair of images captured at t and $(t + \Delta t)$, where Δt is the time interval between the two image frames.

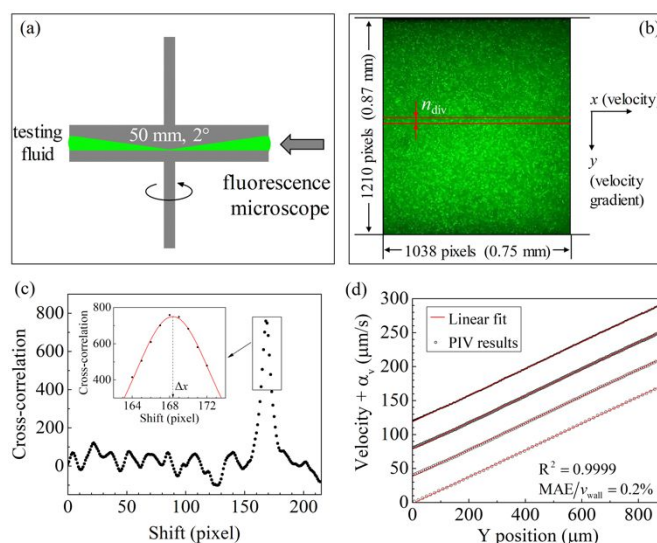


Fig. 1 Illustration of the instrument and algorithm for PIV calculation. (a) Schematic diagram of the geometry and the setup of the microscope. See the supplementary materials for a more detailed diagram. (b) An image of the shearing cell loaded with the control fluid. Red lines show an image stripe, and n_{div} denotes its height in unit of pixels. The coordinates ($x = 0$, $y = 0$) correspond to the pixel on the left upper corner of the image. $y = 0$ indicates the boundary of the upper cone, and $y = 1210$ pixels that of the bottom plate. (c) Cross-correlation of the rescaled 1D brightness fluctuation obtained from a pair of image stripes ($\Delta t = 0.695$ s) in the region of $1205 \leq y \leq 1210$. The insert shows the Gaussian fitting of the 9 data points around the global maximum. (d) Velocity profiles in the control fluid under constant shear at 0.2 s⁻¹. The four sets of results are shifted vertically with the shifting factors $\alpha_v = 120, 80, 40, 0$ $\mu\text{m/s}$ from up to bottom. Black symbols are experimental results with $n_{div} = 1, 5, 10$, and 20 pixels from up to bottom. Red lines are the linear fits of the experimental data. R^2 : coefficient of determination of the linear fits. MAE: mean absolute error. v_{wall} : the velocity of the moving wall.

We set $\Delta t \approx 1/(10\dot{\gamma}_0)$ in our calculation, where $\dot{\gamma}_0$ is the apparent shear rate. The exact value of Δt slightly varies around this value and is determined through the timestamps of the two frames. We crop the images and keep only the region sandwiched between the upper cone ($y = 0$) and bottom plate ($y = H$). After cropping, the images have a size of 1210×1038 pixels (height \times width), which corresponds to a physical dimension of 0.87×0.75 mm. A larger field of view (FOV) can be achieved by using objectives with smaller magnifications. For example, in the experiments of Fig. S9, we use a larger FOV (2.6×0.873 mm) to examine the flow heterogeneity along the flow direction. The size of the FOV does not have significant impact on the PIV results unless v_x shows a large variation with x within the FOV.

Next, we use the contrast-limited adaptive histogram equalization (CLAHE) algorithm³⁰ to increase image contrast (Fig. S2). We index all pixels according to their coordinates on the image. The origin is set as the pixel on the left upper corner. We then divide the pair of images into adjacent horizontal stripes with a height of n_{div} pixels, as shown in Fig. 1(b). We calculate the brightness intensity fluctuation (BIF) along x in each stripe, $I_k(x)$, according to

$$I_k(x) = \sum_{y=n_{\text{div}}(k-1)}^{n_{\text{div}}k-1} I(x,y), \quad (2)$$

where $k = 1, 2, \text{etc.}$ is the index of the stripes and $I(x,y)$ is the brightness intensity (ranging from 0 to 255) of the pixel at (x,y) . $I_k(x)$ is then linearly rescaled to the range of $(-1,1)$. The cross-correlation of the rescaled BIF of the two stripes reaches a maximum at a shift value that equals to the average displacement (Δx) of the tracer particles in the stripes, as shown in Fig. 1(c). Δx can be further refined with sub-pixel precision by fitting the adjacent data points around the maximum with a Gaussian function. The average velocity of tracer particles in the stripe equals $\Delta x/\Delta t$. Repeating this process for all stripes across the gap gives the velocity profile $v_x(y,t)$.

This PIV algorithm has high spatial resolution; the stripe thickness can be as small as a single pixel ($n_{\text{div}} = 1$), which gives a spatial resolution of $0.7 \mu\text{m}$ in the measurement of Fig. 1(b). We set $n_{\text{div}} = 5$ in the PIV calculation of the fumed silica suspension. Fig. 1(d) shows that the instantaneous velocity profiles $v_x(y,t)$ in the control fluid are very close to the theoretical values. The values of R^2 (coefficient of determination) for all four fits are 0.9999. And the mean absolute errors (MAE) for all four fits are as small as 0.2% of the wall velocity. The MAE is defined as

$$\text{MAE} = \frac{1}{N} \sum_{k=1}^N |v_x(y_k) - v_x(y_k)|, \quad (3)$$

where y_k indicates the y coordinate of the center of the k^{th} image stripe, $v_x(y_k)$ is the average velocity along the flow direction of the k^{th} image stripe, and N is the total number of image stripes. The high value of the R^2 (close to unity) and the small value of the MAE indicate that the PIV algorithm has high accuracy. We also calculated the velocity profile using the two-dimensional PIV algorithm proposed by Thielicke³¹ and confirm

that the velocity along the gradient direction is negligible (Fig. S3). In this work we mainly use the 1D PIV algorithm because it has higher spatial resolution than the 2D method does and it is less compute-intensive. We use the 2D method to repeat a fraction of the calculation to confirm the validity of the 1D algorithm.

Experimental results

Shear startup tests

We first examine the evolution of the local velocimetry in shear startup tests. The test procedure consists of three steps – (1) a pre-shear at a shear rate of 200 s^{-1} for 2 minutes, (2) a rest period (the shear rate decreases from 200 to 0 s^{-1} within 20 s and remains at 0 s^{-1} for a duration of $t_w = 10$ min), and (3) a shear startup with an apparent shear rate of $\dot{\gamma}_0$ and a duration of t_s . The purpose of the pre-shear is to create a reproducible starting state by shearing the sample at a large shear rate. Internal structures of the material gradually develop during the rest period, and slowly break down after a sudden shear startup. The growth of the moduli after the preshear is presented in Fig. S15. The focus of this section is to investigate the rheological response and the evolution of shear inhomogeneities after the sudden shear startup at different shear rates. We briefly discuss how t_w influences the rheological response and the dynamics of the velocity gradient in Fig. 6.

The rheological measurement gives the stress transients, $\sigma(t, \dot{\gamma}_0)$, and the PIV analysis provides the evolution of the local velocity profiles, $v_x(y,t)$. To examine the dynamics of the velocity gradient inhomogeneities, we use two variables, ϕ_v and $\phi_{\dot{\gamma}}$, to quantify the instantaneous level of flow heterogeneity. ϕ_v is defined as

$$\phi_v = \int_0^H \frac{2}{H} \left| \frac{v_x(y,t)}{H} - \frac{y}{H} \right| dy, \quad (4)$$

where H denotes the size of the gap. By this definition, ϕ_v equals two times the total absolute area between the normalized velocity profile and that of a homogeneous flow (i.e., a straight line, $v_x(y) = \dot{\gamma}_0 y$). $\phi_v = 0$ for a uniform shear flow and $\phi_v = 1$ for a plug flow with $v_{\text{plug}} = 0$ or $\dot{\gamma}_0 H$. Due to noise in experiments and limited resolution of the camera, we take the threshold $\phi_v < 0.05$ as a criterion for a uniform flow.

$\phi_{\dot{\gamma}}$ is defined as

$$\phi_{\dot{\gamma}} = \Delta \dot{\gamma} / \dot{\gamma}_0, \quad (5)$$

where $\Delta \dot{\gamma} = \dot{\gamma}_{\text{max}} - \dot{\gamma}_{\text{min}}$ is the difference between the maximum and the minimum local shear rates for an instantaneous velocity profile. $\Delta \dot{\gamma}$ and hence $\phi_{\dot{\gamma}}$ are zero in a uniform shear flow. Calculation of local shear rates requires differentiation of velocity profiles. To avoid large errors in numerical differentiation, we divide each velocity profile into ten adjacent regions across y and calculate the local shear rates through linear fitting, which gives a smoothed approximation of $\Delta \dot{\gamma}$.

ϕ_v and $\phi_{\dot{\gamma}}$ quantify the level of flow heterogeneity from two different perspectives. ϕ_v depends on the whole velocity profile

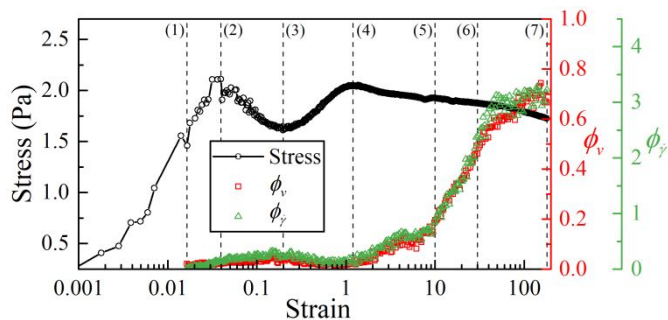


Fig. 2 Evolutions of the stress, and flow inhomogeneity metrics ϕ_v , and ϕ_γ in a shear startup test ($\dot{\gamma}_0 = 0.01 \text{ s}^{-1}$). Dashed lines indicate the strain values (0.016, 0.04, 0.2, 1.2, 10, 30, 180) at which the instantaneous velocity profiles are plotted in Fig. 3. Test procedure: the sample is first sheared at 200 s^{-1} for 2 min; the shear rate then decreases to zero within 20 s; after a rest period of duration 10 min, the shear rate instantly jumps to $\dot{\gamma}_0$ and is held constant for a duration of $t_s = 5 \text{ hrs}$. The total strain $\gamma_{\text{tot}} = \dot{\gamma}_0 t_s = 180$.

rather than just the local shear rates. It is sensitive to wall-slip. In contrast, ϕ_γ only depends on the maximum variation of the shear rate. It does not consider the effects of wall-slip. A linear velocity profile with strong wall-slip would give a large value of ϕ_v but a zero value of ϕ_γ . Our experimental results show negligible slip.

Fig. 2 shows the evolution of the stress, as well as of ϕ_v and ϕ_γ in a shear startup test with $\dot{\gamma}_0 = 0.01 \text{ s}^{-1}$. The stress first gradually increases and reaches a maximum at around 0.04 strain units. The stress then decreases but soon starts to grow again until the second peak at around one strain unit, after which the stress exhibits a slow decay. The first peak and the subsequent decrease in the stress transients indicate a yielding response of the material, which agrees with the results of a dynamic strain sweep test (Fig. S13). The crossover of the elastic and loss moduli curves occurs at a strain amplitude of about 0.04 strain units, very close to the strain value of the first stress overshoot in Fig. 2. The growth of the stress after the first stress overshoot indicates a hardening response – the stress it takes to maintains the constant shear rate of 0.01 s^{-1} gradually increases.

The characteristic strains determined from the rheological response can also be seen in the evolution of the velocity profiles. For convenience of discussion, we marked out seven strain values ($\gamma_1, \gamma_2 \dots \gamma_7$) as indicated by the dashed line in Fig. 2. The instantaneous velocity profiles at those strain values are shown in Fig. 3. The flow remains uniform for $\gamma < \gamma_2$, and the inhomogeneity slightly grows for $\gamma_2 < \gamma < \gamma_3$. The flow inhomogeneity, however, stops growing and decreases

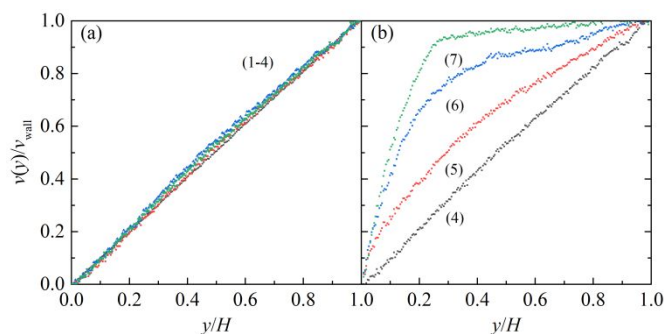


Fig. 3 Instantaneous velocity profiles (normalized by H and $v_{\text{wall}} = \dot{\gamma}H$) at the strain values as indicated in Fig. 2.

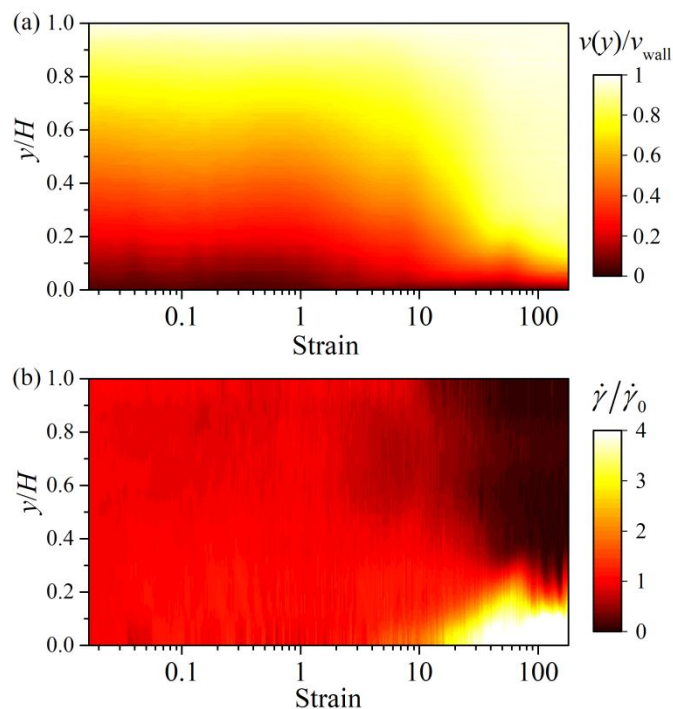


Fig. 4 Position-strain plot of (a) the velocity profile (normalized by H and v_{wall}) and (b) the local shear rate (normalized by $\dot{\gamma}_0$) in the shear startup test with $\dot{\gamma}_0 = 0.01 \text{ s}^{-1}$. Background color indicates the level of velocity or shear rate according to the corresponding color bar on the right.

between γ_3 and γ_4 . After γ_4 the flow inhomogeneity starts to grow continuously, and two distinct shear bands eventually form, as shown in Fig. 3(b). The sample shows no noticeable wall-slip throughout this and other experiments reported here.

The non-monotonic evolution of ϕ_v and ϕ_γ in Fig. 2 suggests that the flow undergoes transitions from unstable (from γ_1 to γ_3) to stable (from γ_3 to γ_4) and then again to unstable dynamics (from γ_4 to γ_7). This finding agrees nicely with available theory for the triggers of shear banding in time-dependent flows^{8, 10} – namely, that stress overshoot and subsequent stress decay can often lead to linearly unstable dynamics and trigger growth of flow heterogeneity. Another interesting finding in Fig. 2 is that ϕ_v and ϕ_γ show a very similar evolution. We find that the local flow inhomogeneity, $\delta\dot{\gamma}(y,t)$, defined by Eq.(6), follows a similar pattern of growth across the shear cell.

$$\delta\dot{\gamma}(y,t) = \dot{\gamma}(y,t) - \dot{\gamma}_0. \quad (6)$$

A master curve of growth can be constructed for $\delta\dot{\gamma}(y,t)$ at different y positions, as shown in Fig. S12. Lack of wall-slip and similarity in the local kinetics of $\delta\dot{\gamma}$ across the shear cell are likely what cause the similar evolution of ϕ_v and ϕ_γ .

The spatiotemporal evolution of the velocity and the local shear rate are presented in Fig. 4, which shows how flow instability grows in this experiment. The local shear rate profiles are calculated by differentiating the smoothing spline (s) of the normalized velocity profiles. The smoothing spline minimizes the objective function f_{obj} defined as

$$f_{\text{obj}} = p \sum_k [\bar{v}_k - s(\bar{y}_k)]^2 + (1-p) \int \left(\frac{d^2 s}{dy^2} \right)^2 dy, \quad (7)$$

where p is the smoothing factor and is set to 0.995. $\bar{v}_k = v_k/(\dot{\gamma}_0 H)$ is the normalized velocity of the k^{th} data point on a velocity profile and $\bar{y}_k = y_k/H$ is the normalized y position of this data point.

Next, we examine the rheological response and dynamics of the velocity profile in a set of shear startup tests with various apparent shear rates. Fig. 5 (a) shows that as the shear rate increases, both the first stress overshoot and the corresponding strain increase. The second stress overshoot, however, becomes less obvious and reduces to a kink in the stress transient. The first stress overshoot in all those experiments are not caused by inertia effects (time scale for fluid inertia is about 4 μs) or the lag of response of motor. We confirm that the actual shear rate imposed on the sample is close to the nominal shear rate (Fig. S16). Figs. 5 (b) and (c) show the evolution of respectively ϕ_v and $\phi_{\dot{\gamma}}$ in corresponding shear startup tests. ϕ_v and $\phi_{\dot{\gamma}}$ show similar transient responses in all seven tests. As the apparent shear rate increases, the overall levels of ϕ_v and $\phi_{\dot{\gamma}}$ decrease. Above a critical value of the shear rate between 0.1 and 0.25 s^{-1} the flow remains uniform. The nonmonotonic growth pattern seen in the test of $\dot{\gamma} = 0.01 \text{ s}^{-1}$ also occurs for shear rates of 0.025, 0.05, and 0.1 s^{-1} . This robust behavior demonstrates the strong correlation between the rheological

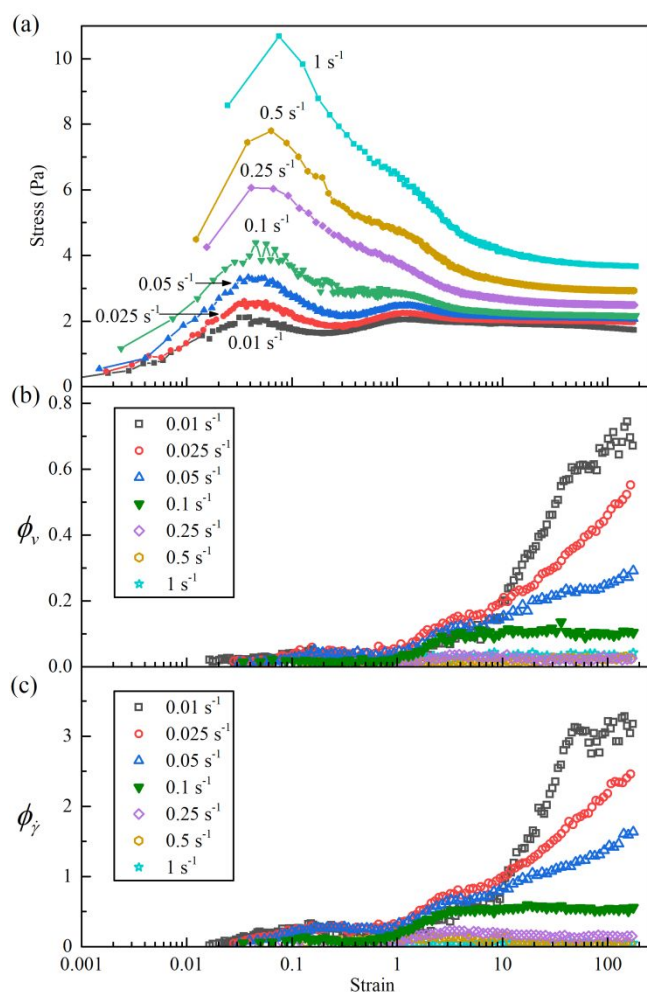


Fig. 5 The evolution of (a) the stress, (b) ϕ_v , and (c) $\phi_{\dot{\gamma}}$ with the shear strain in a set of shear startup tests.

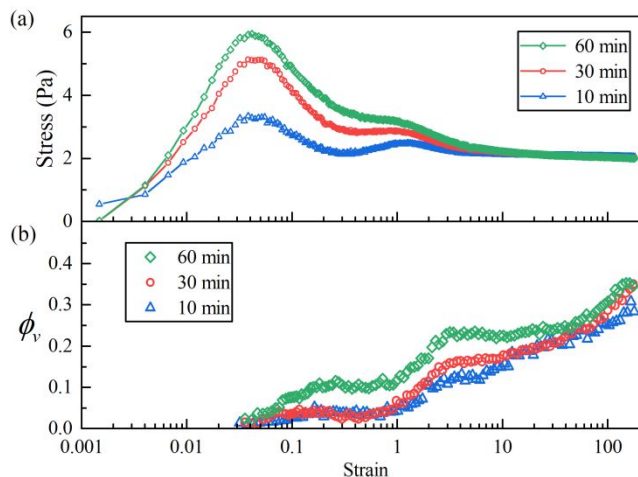


Fig. 6 The evolution of (a) the stress and (b) ϕ_v with shear strain in three shear startup tests with $\dot{\gamma}_0 = 0.05 \text{ s}^{-1}$ and $t_w = 10, 30,$ and 60 min .

response and the velocity profile dynamics. One key feature in Fig. 5 is that the growth of ϕ_v and $\phi_{\dot{\gamma}}$ mainly occurs after the second stress overshoot (or at the kink on the stress evolution curve) which lies at around two strain units.

This behavior also occurs consistently for different waiting times (t_w) between the preshear and the shear startup. Fig. 6 shows the evolution of the stress and ϕ_v in three shear startup tests with $\dot{\gamma}_0 = 0.05 \text{ s}^{-1}$ and $t_w = 10, 30,$ and 60 min . Although we present only the data of ϕ_v for brevity, ϕ_v and $\phi_{\dot{\gamma}}$ again show similar evolution. After the preshear, the suspension's moduli slowly build up following a logarithmic relaxation with time (Fig. S15). The rheological response after the shear startup is sensitive to t_w . As t_w increases, the first stress overshoot increases while the second one becomes less significant. The stress approaches the same level after around 10 strain units, as shown in Fig. 6(a). The evolution of ϕ_v for $t_w = 10$ is similar to that for $t_w = 30 \text{ min}$. While for $t_w = 60 \text{ min}$, ϕ_v rises more quickly and remains at slightly higher values after shear startup than in the other two tests. But ϕ_v eventually approaches the same level in the three experiments.

Gradual growth of shear bands or flow heterogeneities in shear startup tests have also been seen in other systems. One example is a thixotropic Laponite suspension studied by Martin and Hu¹⁴. They found that the flow forms two distinct bands. They observed three different evolution pathways of shear bands depending on flow conditions: 1) the low-shear-rate band expands in spatial width and eventually forms a steady band; 2) the high-shear-rate band gradually expands to a steady-state band; 3) the high-shear-rate band completely fills the domain, leading to a homogeneous flow. The authors found that the pathway followed is determined by two factors: 1) the relative magnitude of the apparent shear rate ($\dot{\gamma}_0$) relative to a critical shear rate ($\dot{\gamma}^*$); 2) the relative value of the stress ($\sigma(t)$) to the static yield stress (σ^*). Regardless of aging time, when $\dot{\gamma}_0 < \dot{\gamma}^*$, Pathway 1) or 2) occurs; otherwise, 3) occurs. Pathway 1) occurs when the high-shear-rate band has a local shear rate ($\dot{\gamma}^H$) smaller than $\dot{\gamma}^*$. Pathway 2) occurs when $\dot{\gamma}^H > \dot{\gamma}^*$ and the local yield stress in the low-shear-rate bands grows larger than σ^* . The flow heterogeneity dynamics in our fumed silica

suspension also shows Pathways 1) and 3). The decrease of flow heterogeneity in the region showing noticeable hardening-like response in our studies is similar to Pathway 3), and the growth of flow heterogeneity after the second stress overshoot is similar to Pathway 1) found in the Laponite suspension. A key difference between the two systems is that in the fumed silica suspension, Pathways 1) and 3) occur in the same shear startup test but at different strains while in the Laponite suspension, the two features are seen in different experiments.

Other examples showing gradual growth of shear bands include wormlike micelles reported in the work of Hu and Lips¹⁷ and entangled star polymers studied by Rogers et al.¹⁸ as briefly reviewed in the Introduction. The growth of shear bands in the wormlike micelles was traced to micelle entanglement/disentanglement dynamics, and that in entangled star polymers to the formation of repulsive soft particles. The fumed silica suspension shows more complicated dynamics of shear rate inhomogeneities that exhibits clear correlation with the non-monotonic stress evolution. This phenomenon indicates multiple types of structural changes under continuous shearing. As will be discussed later, flow reversal tests and constitutive modeling further consolidate this scenario.

Note that ϕ_v and $\phi_{\dot{\gamma}}$ do not reach plateau values at the end of the experiments with apparent shear rates of 0.025 and 0.05 s^{-1} . We limit the maximum strain in the set of shear startup experiments to around 180 strain units because in a sample prepared as described in the supplementary materials (Section 3), we observed that over long periods of shearing (over 2000 strain units at 0.075 s^{-1}), the sample did not show a steady velocity profile but instead exhibits noticeable velocimetry oscillation. We found that the oscillation is triggered by a slight geometry misalignment and is in phase with the rotation of the

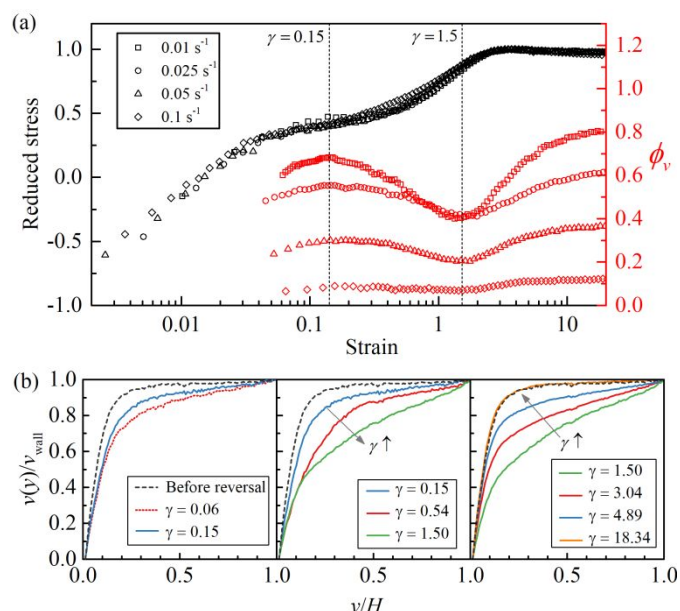


Fig. 7 (a) Evolution of the stress, normalized by the absolute stress before flow reversal, and ϕ_v in a set of flow reversal tests. (b) Instantaneous velocity profiles in the flow reversal test with $\dot{\gamma}_0 = 0.01 s^{-1}$. Dashed black lines in all three panels indicate the velocity profile before shear reversal. Lines in color are the velocity profiles after shear reversal with corresponding strain values indicated in the legend.

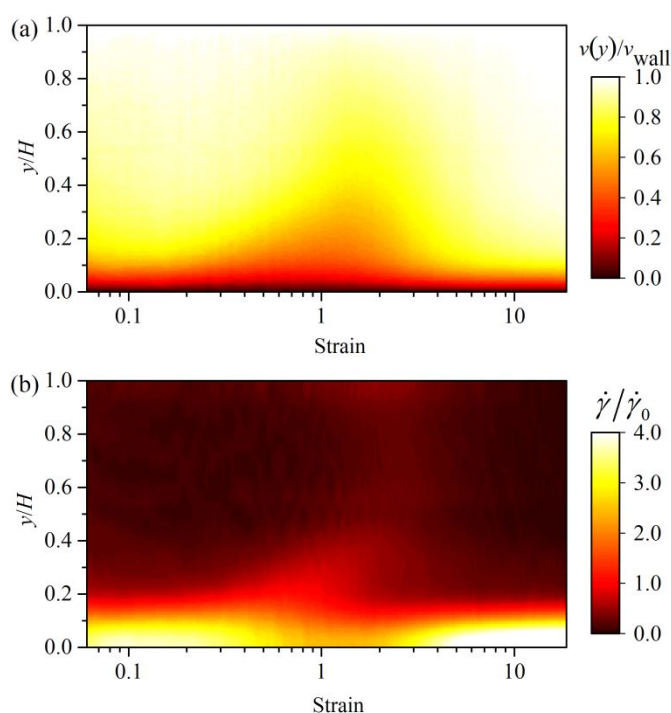


Fig. 8 Position-strain plot of (a) the velocity profile (normalized by H and v_{wall}) and (b) the local shear rate (normalized by $\dot{\gamma}_0$) in the flow reversal test with $\dot{\gamma}_0 = 0.01 s^{-1}$. Background color indicates the level of velocity or shear rate according to the corresponding color bar on the right.

geometry. The amplitude of oscillation slowly grows with time. We observed two-dimensional heterogeneity as the oscillation becomes stronger. The velocity profile in the PIV observation window oscillates periodically as the shear rate variation across the gap, carried by the geometry, crosses in and out of the field of view. We characterized the geometry misalignment and showed that it is within the range of manufacturing error. In contrast to the fumed silica suspension, velocimetry oscillation in the Newtonian control fluid is negligible and does not grow with time. Thus, we believe that such oscillations in velocity profile may be common in TYSFs, triggered by miniscule imperfections in geometry. We note that the pronounced oscillation in velocity gradient induced by misalignment shows hardly any signature in the measured shear stress. Thus, without a measurement of the velocity field, neither the oscillatory velocity profile nor the misalignment that causes it, would be evident from the bulk rheology. Further discussion of velocimetry oscillation can be found in the supplementary materials (Section 3).

Shear reversal tests

In this section, we investigate the response of the inhomogeneous flow to a sudden reversal of the shearing direction. In purely viscous fluids, including ideal thixotropic fluids, the stress $\sigma(t)$ and the velocity profile $v_x(y,t)$ instantly flip to respectively $-\sigma(t)$ and $-v_x(y,t)$ when the shearing direction reverses (neglecting fluid inertia). The fumed silica suspension, however, show different behaviors. Fig. 7(a) shows the rheological response and the evolution ϕ_v in a set of flow reversal experiments in which $\dot{\gamma}$ suddenly jumps from $-\dot{\gamma}_0$ to

$\dot{\gamma}_0$ at $\gamma = 0$. $\phi_{\dot{\gamma}}$ follows a similar evolution as ϕ_v in all four experiments. Denoting the stress before the flow reversal as σ_- , the reduced stress, $-\sigma/\sigma_-$, can be scaled with the strain to yield a master curve, shown in Fig. 7(a). The initial steep response and the first turning point lie within the same strain range as the that of first stress overshoot in shear startup experiments. The second turning point on the master curve lies within the same strain range as that of the second stress overshoot in shear startup experiments.

The dynamics of the velocity gradient heterogeneity in flow reversal exhibit a strong dependence on the strain. In the four experiments shown in Fig. 7(a), ϕ_v first slightly increases for $\gamma < 0.15$, then decreases with the strain until $\gamma = 1.5$, after which ϕ_v slowly rises and approaches the value before flow reversal. Fig. 7(b) shows several velocity profiles in the flow reversal test with $\dot{\gamma}_0 = 0.01 \text{ s}^{-1}$. After flow reversal, the velocity profile undergoes a sudden but slight homogenization, which can be seen by comparing the velocity profile at $\gamma = 0.06$ with that before flow reversal. The velocity profile then evolves towards the shape before flow reversal until $\gamma = 0.15$, after which a second homogenization of the velocity profile starts. This homogenization ends at around 1.5 strain units. ϕ_v grows again afterwards, and the velocity profile eventually reaches the same shape prior to flow reversal. Fig. 8 shows a position-strain map of the velocity and the shear rate in this flow reversal test.

Comparison of the results in shear startup tests depicted in Fig. 5 with those from the shear reversal tests in Fig. 7 reveals an important finding: the regions of around $0.2 < \gamma < 2$ in the two types of tests are both governed by a hardening-like response (the stress it takes to maintain a constant apparent shear rate increases with strain) which tends to suppress flow heterogeneity. In shear startup tests, this hardening-like response keeps the flow uniform until thixotropy becomes dominant. In flow reversal tests, it leads to a temporary homogenization of the flow, and as it slows down, flow heterogeneity grows again.

This hardening-like response is very similar to the Bauschinger effect³² that many polydomain solids such as metals exhibit³²⁻³⁶. The Bauschinger effect refers to the phenomenon that plastic deformation leads to the formation of an anisotropic yield stress – the yield stress increases in the straining direction with a consequent decrease in the opposite direction, and the change of yield stress can be reversed by straining toward the opposite direction. And upon continued straining in the opposite direction, hardening eventually occurs in that direction as well. The term “kinematic hardening” is often used to describe this phenomenon, in contrast with “isotropic hardening,” which is an increase in yield stress in all directions upon straining in one direction. We refer the readers to our recent review for a further explanation³⁷.

Constitutive modeling

Proposed model

We now present a minimal model consisting of kinematic hardening and thixotropy and show that it can qualitatively predict the main features of the velocity gradient dynamics in the shear startup tests and flow reversal tests. We assume that the shear rate ($\dot{\gamma}$) depends on the stress (σ) and two structural variables, A and λ , according to the following constitutive equation:

$$\dot{\gamma} = \frac{\text{sign}(\sigma_{\text{eff}}) \max[|\sigma_{\text{eff}}| - \lambda\sigma_{y0}, 0]}{(\eta_{\text{th}}\lambda + \eta_n)}, \quad (8)$$

where $\sigma_{\text{eff}} = \sigma - CA$ and C is a constant model parameter. Here, A is the kinematic hardening parameter and λ is the thixotropic parameter. A and λ account for two aspects of the internal structures – respectively, the level of anisotropy and the overall degree of aggregation. According to Eq. (8), this system has an anisotropic yield surface in stress space $[CA - \lambda\sigma_{y0}, CA + \lambda\sigma_{y0}]$. The yield stress equals $CA + \lambda\sigma_{y0}$ in the positive direction and $CA - \lambda\sigma_{y0}$ in the negative direction. The model does not include elasticity. It predicts a rigid solid for stress within the yield surface.

$\lambda = 1$ and $A = 0$ at the fully structured and isotropic state, but gradually change under flow. Two kinetic equations are needed to describe their evolution with time. We assume that the evolutions of λ follows

$$\dot{\lambda} = -K|\dot{\gamma}\lambda + k_{\lambda}(1 - \lambda), \quad (9)$$

where K and k_{λ} are two model parameters. The terms on the right side of Eq. (9) account for, respectively, the rate of structural breakage and the rate of structural formation.

We assume that the evolution of A follows a kinetic equation defined as

$$\dot{A} = \dot{\gamma} - q(|\dot{\gamma}| + k_A)A, \quad (10)$$

where q and k_A are model parameters. Eq. (10) reduces to the widely-used Armstrong-Frederick (AF) kinematic hardening equation³² when $k_A = 0$. We introduce the relaxation term k_A into this equation because the original AF equation was developed for metals or metallic glasses, and, without the relaxation term, allows the anisotropy in the yield surface to persist indefinitely after cessation of flow. This lack of relaxation is however not appropriate for thixotropic fluids because after flow stops, the microstructure of thixotropic materials can rearrange and consequently restore, at least partially, the isotropic yield surface. The parameter k_A allows A to relax and restore isotropy ($A = 0$) in the absence of shear flow.

At steady state, σ depends on $\dot{\gamma}$ according to

$$\sigma_{\text{ss}}(\dot{\gamma}) = CA_{\text{ss}}(\dot{\gamma}) + \text{sign}(\dot{\gamma})\lambda_{\text{ss}}(\dot{\gamma})\sigma_{y0} + \lambda_{\text{ss}}(\dot{\gamma})\eta_{\text{th}}\dot{\gamma} + \eta_n\dot{\gamma} \quad (11)$$

where $A_{\text{ss}}(\dot{\gamma})$ and $\lambda_{\text{ss}}(\dot{\gamma})$ are defined as follows

$$A_{\text{ss}}(\dot{\gamma}) = \dot{\gamma} / (q|\dot{\gamma}| + k_A), \quad (12)$$

$$\lambda_{\text{ss}}(\dot{\gamma}) = (K|\dot{\gamma}|/k_{\lambda} + 1)^{-1}. \quad (13)$$

$A_{\text{ss}}(\dot{\gamma})$ increases with $\dot{\gamma}$ and approaches a plateau value of $\text{sign}(\dot{\gamma})/q$ when $q|\dot{\gamma}| \gg k_A$. $\lambda_{\text{ss}}(\dot{\gamma})$ decreases with $\dot{\gamma}$ and ranges between unity (when $\dot{\gamma} = 0$) and zero (when $|\dot{\gamma}| \rightarrow \infty$). If we consider only positive shear rates, as $\dot{\gamma}$ increases, the second

term on the right hand side of Eq. (11) decreases, and the other three terms increase. Eq. (11) can be non-monotonic for certain parameter values.

This model is a simplified version of our recent thixotropic elasto-viscoplastic (TEVP) model²⁵. It contains only a single mode of thixotropic relaxation while the full TEVP model introduce a spectrum of thixotropic kinetic equations. Besides, the model presented here uses a simplified kinetic equation for λ that has fewer parameters than that in the TEVP model. Moreover, this simple model does not consider elastic deformation. Another difference is the inclusion of the relaxation parameter k_A in the kinetic equation of A which is absent in our previous TEVP model (as well as all other TEVP models in the literature). We study this simple model because this work focuses on finding the essential components of TEVP rheology that are required to qualitatively predict the major features of heterogeneous shearing and banding dynamics in shear startup and flow reversal tests. A discussion of the eight parameters of the model and how their values are set is given in the SI.

Linear stability analysis

We now consider a 1D shear flow where a sample of fluid whose constitutive response follows Eqs. (7-9) is sandwiched between parallel boundaries at $y = \{0, H\}$. Neglecting fluid inertia, σ is therefore constant across y . The local shear rate and the local structure parameters are given by $\dot{\gamma}(y, t)$, $A(y, t)$, and $\lambda(y, t)$. Now consider the situation in which the flow remains at a uniform steady state $(\dot{\gamma}_0, \sigma_0)$ for $t < 0$ and flow heterogeneity $(\delta\dot{\gamma}, \delta A, \delta\lambda)$, defined in Eq. (14), occurs at $t = 0$. The stress σ is held constant at σ_0 for all t .

$$\begin{cases} \delta\dot{\gamma}(y, t) = \dot{\gamma}(y, t) - \dot{\gamma}_0, \\ \delta A(y, t) = A(y, t) - A_{ss}(\dot{\gamma}_0), \\ \delta\lambda(y, t) = \lambda(y, t) - \lambda_{ss}(\dot{\gamma}_0). \end{cases} \quad (14)$$

Inserting $\delta\lambda(y, t)$ and $\delta A(y, t)$ into respectively Eq. (9) and Eq. (10), and replacing $\dot{\gamma}(y, t)$ with the right hand side of Eq. (8), one obtains the equations for $\delta\dot{\lambda}(y, t)$ and $\delta\dot{A}(y, t)$:

$$\dot{\mathbf{s}} = \mathbf{M}_0 \cdot \mathbf{s}, \quad (15)$$

where $\mathbf{s} = [\delta\lambda, \delta A]^T$ and $\dot{\mathbf{s}} = [\delta\dot{\lambda}, \delta\dot{A}]^T$. Here higher-order terms of \mathbf{s} are omitted. \mathbf{M}_0 is the stability matrix evaluated at the steady state of $(\dot{\gamma}_0, \sigma_0)$:

$$\mathbf{M}_0 = \begin{bmatrix} \partial_{\dot{\gamma}} \dot{\lambda}(A, \lambda, \sigma) & \partial_A \dot{\lambda}(A, \lambda, \sigma) \\ \partial_{\dot{\gamma}} \dot{A}(A, \lambda, \sigma) & \partial_A \dot{A}(A, \lambda, \sigma) \end{bmatrix}_{A=A_{ss}(\dot{\gamma}_0), \lambda=\lambda_{ss}(\dot{\gamma}_0), \sigma=\sigma_0}, \quad (16)$$

The functions $\dot{\lambda}(A, \lambda, \sigma)$ and $\dot{A}(A, \lambda, \sigma)$ can be obtained by inserting Eq. (8) into respectively Eq. (9) and Eq. (10). Note that the linear dynamics of the flow heterogeneity is set by the steady state point $(\dot{\gamma}_0, \sigma_0)$ and does not depend on y . This steady state point is linearly unstable under constant stress conditions if \mathbf{M}_0 contains eigenvalues with positive real parts. This is a necessary condition for the occurrence of shear rate inhomogeneity and shear bands under constant stress or constant apparent shear rate.

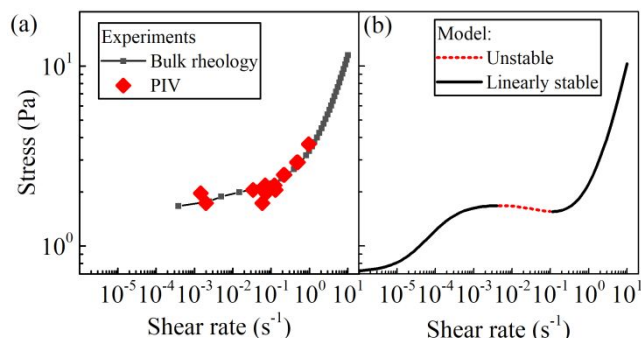


Fig. 9 (a) Pseudo-steady flow curve determined from the bulk rheometry (black symbols) and local velocimetry (red symbols). (b) Model predictions with solid line indicating the linearly stable portion and the dashed line indicating the unstable portion.

This model qualitatively agrees with the experiments. Fig. 9 shows the pseudo-steady flow curve measured through bulk rheometry and through the rheo-PIV technique (stress versus local shear rate). The flow curve was measured by holding the shear stress constant for a duration of t_d at a series of stress values following a linearly increasing order. t_d was set to change from 15 hours for the first data point to 5 minutes for the last data point following a logarithmic spacing. Note that we use the term “pseudo-steady flow curve” because at small apparent shear rate, the flow heterogeneity is still slowly growing when each data point is obtained.

The flow curve in Fig. 9(a) shows that there seemingly exists a region of shear rates, represented by the dashed red line, that is inaccessible for homogeneous flow. Corresponding to this region, the model predicts an unstable region of shear rates where the flow curve has a negative slope. The system forms shear bands if the apparent shear rate remains in this unstable region. Here the parameters were set to the following values to achieve predictions qualitatively similar to the experimental results: $\sigma_{y0} = 0.72$ Pa, $C = 1$ Pa, $\eta_{thi} = 4$ Pa·s, $\eta_n = 0.9$ Pa·s, $k_A = 10^{-4}$ s⁻¹, $k_\lambda = 10^{-3}$ s⁻¹, $q = 1$, $K = 2.5 \times 10^{-3}$. A brief discussion on how the model parameters can be determined is provided in the supplementary materials (Section 7).

Numerical simulation

We solve the model with a single spatial coordinate, namely the velocity gradient direction, to simulate the formation and evolution of shear rate inhomogeneity under transient shear flow. To obtain well defined results with such a 1D model, where there is a clear selection of stress at which inhomogeneities in shear rate grow, Lu et al.³⁸ introduced diffusive terms into their dynamical equations. We follow their procedure by introducing such terms into Eqs. (9) and (10) as follows

$$\partial_t \lambda(t, y) = -K |\dot{\gamma}| \lambda + k_\lambda (1 - \lambda) + D \partial_y^2 \lambda, \quad (17)$$

$$\partial_t A(t, y) = \dot{A} - (|\dot{\gamma}| + k_A) A + D \partial_y^2 A. \quad (18)$$

The spatial gradients $D \partial_y^2 A$ and $D \partial_y^2 \lambda$ allow for smooth velocity profiles at scales larger than $l \propto \sqrt{D}$, which is physically due to interactions across adjacent streamlines. The apparent shear rate, Γ , is set by the test procedure and equals the spatial average of the local shear rate $\dot{\gamma}(y, t)$:

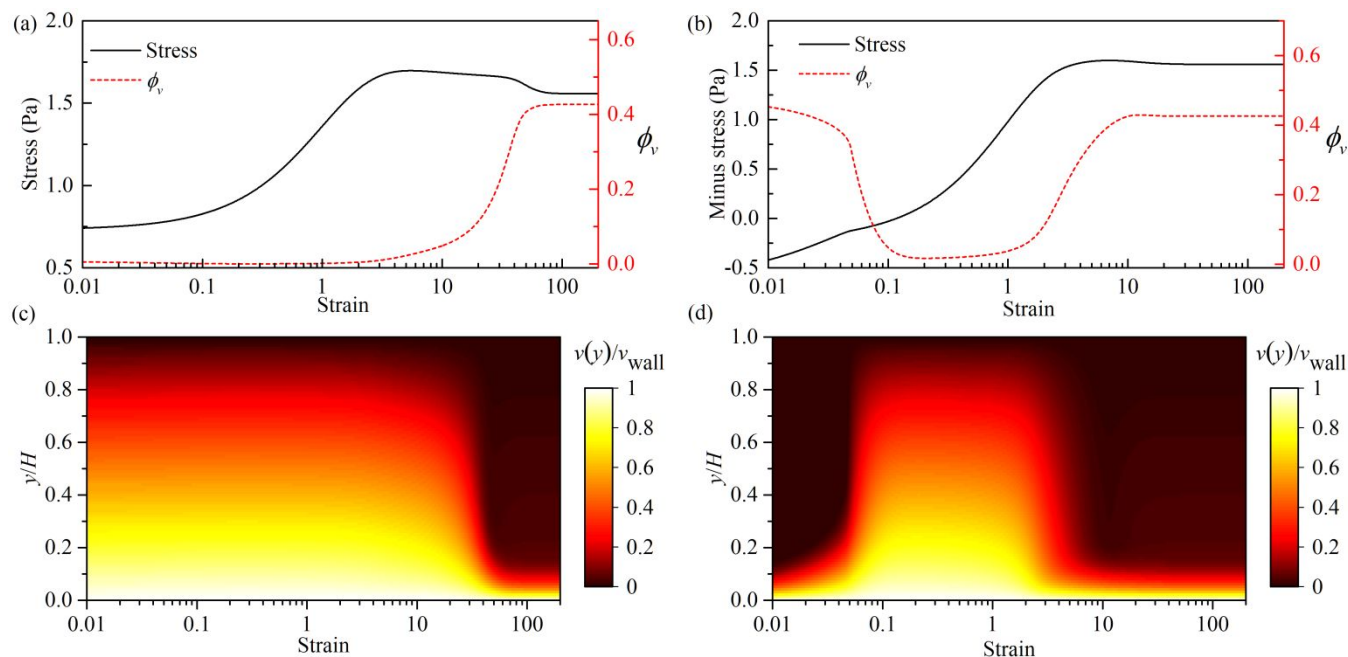


Fig. 10 Numerical simulation of a shear startup test ($\Gamma = 0.01 \text{ s}^{-1}$) followed by a sudden flow reversal ($\Gamma = -0.01 \text{ s}^{-1}$). (a) and (b) show the rheological response and the evolution of ϕ_v in, respectively, the shear startup and flow reversal tests. (c) and (d) show the space-strain plots of the velocity profiles in, respectively, the shear startup and flow reversal tests.

$$\Gamma = \frac{1}{H} \int_0^H \dot{\gamma}(y,t) dy, \quad (19)$$

We solve this model using boundary conditions $\partial_y \sigma = 0$ and $\Gamma = 0.01 \text{ s}^{-1}$, and initial perturbations $A(y, t = 0) = \delta A(y, t = 0)$, $\lambda(y, t = 0) = 1 + \delta \lambda(y, t = 0)$. We set $D = 10 \mu\text{m}^2/\text{s}$, $\delta A(y, t = 0) = a_1 \sin(\omega_1 y)$, and $\delta \lambda(y, t = 0) = a_2 |\sin(\omega_2 y)|$, where $a_1 = a_2 = 0.1$ and $\omega_1 = \omega_2 = 25\pi/H$. We set $H = 1 \text{ mm}$. The other parameters take the same values as used in Fig. 9. We note that the quantitative details of the calculation depend strongly on δA and $\delta \lambda$ but the qualitative features of the evolution of ϕ_v and $\phi_{\dot{\gamma}}$ do not.

Fig. 10 (a) shows the predicted rheological response and the evolution of ϕ_v of a shear startup test (Γ jumps from 0 to 0.01 s^{-1}) and Fig. 10 (b) shows the same for a subsequent flow reversal test (Γ jumps from 0.01 to -0.01 s^{-1}). ($\phi_{\dot{\gamma}}$ shows a similar evolution as ϕ_v .) Note that the constitutive model we use does not include an elastic component and therefore cannot capture the gradual rise of the stress before the first stress overshoot in shear startup tests. However, the model qualitatively captures the kinematic hardening (the increase of the stress for $0.2 < \gamma < 3$) and the later thixotropic response (the stress decay for $\gamma > 3$). The model shows that ϕ_v does not grow until the kinematic hardening response slows down and the thixotropic response becomes dominant. Position-strain plots of the velocity profiles are shown in Figs. 10 (c, d). The model predictions qualitatively agree with the experimental results in Fig. 2.

The impact of the kinematic hardening response on the dynamics of the velocity profile can be seen more clearly in the flow reversal test. Fig. 10 (b) and (d) show that a sudden flow reversal lead to temporary homogenization of the flow. Shear inhomogeneities grow again as the kinematic hardening

response slows down. The model predictions of several more shear startup tests are provided in Fig. 11. The results in Fig. 11(b) clearly show the transition from a stable process in which ϕ_v gradually decreases to an unstable process as the kinematic hardening evolution slows down. The model over-predicts the evolution of ϕ_v for the three experiments with shear rates of 0.025 , 0.05 , and 0.1 s^{-1} .

The apparent flow curve of heterogeneous flow can be obtained through simulation of shear startup tests at a series of apparent shear rates. The apparent flow curve differs from the constitutive flow curve in the linearly unstable region. The rheological curve is sensitive to $\mathcal{D} = D/H^2$ where D is the diffusion coefficient in the model and H is the gap. When \mathcal{D} is small (e.g. 10^{-3}), the flow curve is close to the constitutive flow curve. As \mathcal{D} increases, a flat plateau appears in the linearly

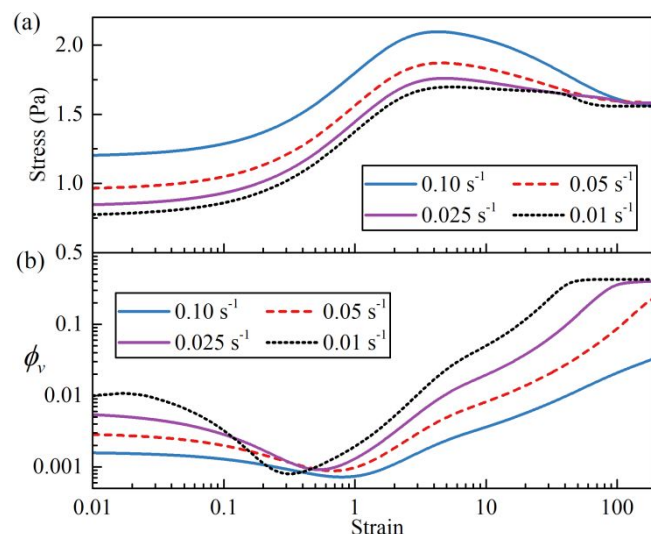


Fig. 11 Model predictions of (a) the rheological response and (b) the evolution of ϕ_v in four shear startup test with apparent shear rates of 0.01 , 0.025 , 0.05 , and 0.1 s^{-1} .

unstable region (Fig. S17). This model exhibits a stress selection mechanism. According to the criterion proposed by Lu et al.³⁸, a model that is “a differential equation and satisfies rotational and Galilean invariance” has a shear-band solution of a “non-transverse saddle connection,” which results in a sharp stress selection – a critical shear stress exists at which a low-shear-rate band coexists with a high-shear-rate band. This sharp stress selection results in a flat plateau on the apparent flow curve of the heterogeneous flow.

Summary and final comments

We have studied how shear inhomogeneities occur and grow in a thixotropic fumed silica suspension in shear startup and flow reversal tests. The material exhibits a critical shear rate below which heterogeneity in the velocity gradient and shear bands occur. The rheological response and the dynamics of the velocity gradient are strongly correlated. In shear startup tests below the critical shear rate, flow heterogeneity exhibits a non-monotonic evolution – it increases as the stress undergoes a first overshoot, and then decreases as a hardening-like behavior occurs, and lastly increases again along with the appearance of a thixotropic shear thinning. In flow reversal experiments, flow heterogeneity also exhibits a non-monotonic evolution – heterogeneity first increases as the stress undergoes a steep increase with strain; it then temporarily decreases in tandem with the hardening response, and lastly it slowly grows again.

We proposed the hypothesis that kinematic hardening and thixotropy are the two main factors governing the dynamics of the velocity gradient, and the former response tends to stabilize the flow while the latter leads to the growth of flow heterogeneity. We tested this hypothesis by constructing a simple thixotropic yield stress model with two dynamical variables – one for thixotropy and the other one for kinematic hardening (KH). As opposed to previous thixotropic KH models, our model allows the KH effect to decay after flow stops. With this simple addition, the model can qualitatively capture the important features of the rheological response and the dynamics of the shear rate heterogeneity in shear startup and flow reversal experiments.

In addition, in a sample prepared as described in the supplementary materials (Section 3), we found that under long periods of shearing at constant apparent shear rates, the velocity gradient periodically oscillates, and the amplitude of oscillation slowly grows with time. Such velocimetry oscillation is triggered by a small geometry misalignment that is within the range of manufacturing error. We observed two-dimensional flow heterogeneity when the velocimetry oscillation is strong. The local shear rate varies along both the flow direction and the gradient direction, and such variation crosses in and out of the field of view carried by the rotating geometry. We measured the geometry misalignment and found that it is within the range of manufacturing error. The geometry misalignment causes very slight velocimetry oscillation in a Newtonian fluid.

This work has a few limitations. 1) We focus on a single particle concentration; how flow heterogeneities and rheology

depend on particle concentration is an important topic for future work. 2) The shear startup tests are limited to around 200 strain units. Extending the durations of those tests may reveal different rheological and banding behaviors. 3) Our PIV technique focuses on mainly one-dimensional velocimetry along the flow direction. The unusual oscillatory velocimetry dynamics in the fumed silica suspension suggests a more complex scenario of how flow heterogeneities occur and evolve under rheometric flow. Future experimental studies may need to extend to two or even three dimensions to thoroughly understand this phenomenon. 4) The constitutive model is purely phenomenologically. Direct measurements or simulations of microstructures are needed to understand the physical mechanism of the rheological responses and flow behaviors of the fumed silica suspension. 5) Fig. S17 shows that after the cessation of pre-shear, the moduli of the suspension gradually grow over several hours, indicating aging. In most of our experiments, the rest period lasts only 10 minutes before shear startup. Thixotropic buildup may be present during the shear startup test. Neither our experimental design nor our modeling takes this into consideration.

Besides those limitations, it has been known that attractive particles such as fumed silica particles can arrange into macroscopic log-rolling flocs under confined geometries³⁹. The recent study by Varga et al.⁴⁰ showed that this phenomenon is very robust and occurs in both microsized aggregates of nanoparticles and non-colloidal particles. Our experiments involve similar flow conditions. Due to the relatively large truncated area of the cone-and-plate geometry used in this work, a significant portion of sample (12 mm in diameter) is sheared with a gap width of 210 μm . We cannot rule out the possibility that such shear-induced structuration occurs in our experiments. Further studies are needed to resolve whether this phenomenon occurs in the fumed silica suspension, and if it does, how it impacts the rheological response and the local velocimetry, including the possibility that it influences what we describe as “kinematic hardening”.

Conflicts of interest

There are no conflicts to declare.

Acknowledgements

The authors thank the Anton Paar Company for providing instruments and the Procter & Gamble Company for financial support, and Will Hartt for inspiring the work in this area and for encouraging support. M.J.S. acknowledges partial support from NSF CBET 1232937 and R.G.L. from NSF CBET 0853662. Any opinions, findings, and conclusions or recommendations expressed in this material are those of the authors and do not necessarily reflect the views of the National Science Foundation (NSF).

Notes and references

1. J. Paredes, N. Shahidzadeh-Bonn and D. Bonn, *Journal of Physics-Condensed Matter*, 2011, **23**.
2. R. Durairaj, N. N. Ekere and B. Salam, *Journal of Materials Science: Materials in Electronics*, 2004, **15**, 677-683.
3. B. C. Blackwell and R. H. Ewoldt, *Journal of Non-Newtonian Fluid Mechanics*, 2016, **227**, 80-89.
4. Y. Wei, M. J. Solomon and R. G. Larson, *Journal of Rheology*, 2016, **60**, 1301-1315.
5. P. Coussot, Q. D. Nguyen, H. T. Huynh and D. Bonn, *Journal of Rheology*, 2002, **46**, 573-589.
6. F. Pignon, A. Magnin and J.-M. Piau, *Physical Review Letters*, 1997, **79**, 4689.
7. J. Vermant and M. J. Solomon, *Journal of Physics-Condensed Matter*, 2005, **17**, R187-R216.
8. S. M. Fielding, *Journal of Rheology*, 2016, **60**, 821-834.
9. R. L. Moorcroft, M. E. Cates and S. M. Fielding, *Physical Review Letters*, 2011, **106**, 4.
10. R. L. Moorcroft and S. M. Fielding, *Physical Review Letters*, 2013, **110**, 5.
11. R. Radhakrishnan and S. M. Fielding, *Journal of Rheology*, 2018, **62**, 559-576.
12. T. Divoux, V. Grenard and S. Manneville, *Physical Review Letters*, 2013, **110**, 018304.
13. T. Divoux, D. Tamarii, C. Barentin and S. Manneville, *Physical Review Letters*, 2010, **104**, 208301.
14. J. D. Martin and Y. T. Hu, *Soft Matter*, 2012, **8**, 6940-6949.
15. C. J. Dimitriou and G. H. McKinley, *Soft Matter*, 2014, **10**, 6619-6644.
16. A. Kurokawa, V. Vidal, K. Kurita, T. Divoux and S. Manneville, *Soft Matter*, 2015, **11**, 9026-9037.
17. Y. T. Hu and A. Lips, *Journal of Rheology*, 2005, **49**, 1001-1027.
18. S. A. Rogers, D. Vlassopoulos and P. Callaghan, *Physical review letters*, 2008, **100**, 128304.
19. R. Radhakrishnan and S. M. Fielding, *Physical Review Letters*, 2016, **117**, 5.
20. R. Radhakrishnan, T. Divoux, S. Manneville and S. M. Fielding, *Soft Matter*, 2017, **13**, 1834-1852.
21. S. M. Fielding, *Reports on Progress in Physics*, 2014, **77**, 15.
22. K. Martens, L. Bocquet and J.-L. Barrat, *Soft Matter*, 2012, **8**, 4197-4205.
23. M. J. Armstrong, A. N. Beris, S. A. Rogers and N. J. Wagner, *Journal of Rheology*, 2016, **60**, 433-450.
24. P. M. Mwasame, A. N. Beris, R. B. Diemer and N. J. Wagner, *AIChE Journal*, 2016, **63**, 517-531.
25. Y. Wei, M. J. Solomon and R. G. Larson, *Journal of Rheology*, 2018, **62**, 321-342.
26. K. Dullaert and J. Mewis, *Rheologica Acta*, 2005, **45**, 23-32.
27. K. Dullaert and J. Mewis, *Journal of Colloid and Interface Science*, 2005, **287**, 542-551.
28. K. Dullaert and J. Mewis, *Journal of Rheology*, 2005, **49**, 1213-1230.
29. K. Dullaert and J. Mewis, *Journal of Non-Newtonian Fluid Mechanics*, 2006, **139**, 21-30.
30. K. Zuiderveld, *Contrast limited adaptive histogram equalization*, Academic Press Professional, Inc., 1994.
31. W. Thielicke and E. Stamhuis, *Journal of Open Research Software*, 2014, **2**.
32. C. O. Frederick and P. Armstrong, *Materials at High Temperatures*, 2007, **24**, 1-26.
33. S. Buckley and K. Entwistle, *Acta Metall.*, 1956, **4**, 352-361.
34. B. Chun, J. Jinn and J. Lee, *Int. J. Plast.*, 2002, **18**, 571-595.
35. R. Milligan, W. Koo and T. Davidson, *Journal of Basic Engineering*, 1966, **88**, 480-488.
36. Y. Xiang and J. Vlassak, *Acta Mater.*, 2006, **54**, 5449-5460.
37. R. G. Larson and Y. Wei, *Journal of Rheology*, 2019, **63**, 477-501.
38. C.-Y. D. Lu, P. D. Olmsted and R. Ball, *Physical Review Letters*, 2000, **84**, 642.
39. A. S. Negi and C. O. Osuji, *Rheologica acta*, 2009, **48**, 871-881.
40. Z. Varga, V. Grenard, S. Pecorario, N. Taberlet, V. Dolique, S. Manneville, T. Divoux, G. H. McKinley and J. W. Swan, *Proceedings of the National Academy of Sciences*, 2019, **116**, 12193-12198.